

See discussions, stats, and author profiles for this publication at: <https://www.researchgate.net/publication/236101517>

Microfluidic Space-Domain Time-Resolved Emission Spectroscopy of Terbium(III) and Europium(III) Chelates with Pyridine-2,6-Dicarboxylate

ARTICLE in ANALYTICAL CHEMISTRY · APRIL 2013

Impact Factor: 5.64 · DOI: 10.1021/ac400200x · Source: PubMed

CITATIONS

6

READS

47

12 AUTHORS, INCLUDING:



Srigokul Upadhyayula

Harvard Medical School / Boston Children's H...

23 PUBLICATIONS 170 CITATIONS

SEE PROFILE



Prashanthi Vandurangi

University of California, Riverside

9 PUBLICATIONS 23 CITATIONS

SEE PROFILE



Sharad Gupta

Indian Institute of Technology Kanpur

29 PUBLICATIONS 181 CITATIONS

SEE PROFILE



Valentine Vullev

University of California, Riverside

76 PUBLICATIONS 955 CITATIONS

SEE PROFILE

Microfluidic Space-Domain Time-Resolved Emission Spectroscopy of Terbium(III) and Europium(III) Chelates with Pyridine-2,6-Dicarboxylate

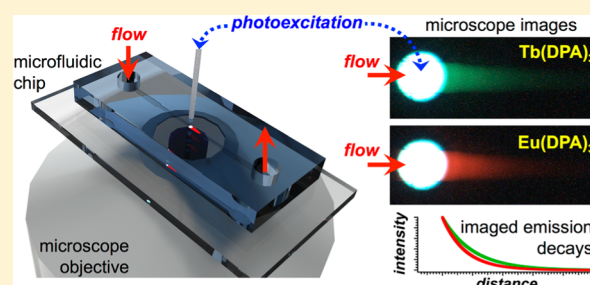
Vicente Nuñez,[†] Srigokul Upadhyayula,^{†,‡} Brent Millare,^{†,||} Jillian M. Larsen,[†] Ali Hadian,[†] Sanghoon Shin,[†] Prashanthi Vandrangi,[†] Sharad Gupta,[†] Hong Xu,[†] Adam P. Lin,[†] Georgi Y. Georgiev,^{†,⊥} and Valentine I. Vullev^{*,†,‡,§}

[†]Department of Bioengineering and Center for Bioengineering Research, University of California, Riverside, California 92521, United States

[‡]Department of Biochemistry, University of California, Riverside, California 92521, United States

[§]Department of Chemistry, University of California, Riverside, California 92521, United States

ABSTRACT: This article describes the utilization of laminar microflows for time-resolved emission measurements with steady-state excitation and detection. Passing a laminar flow through a short illuminated section of a microchannel provided a means for pulsed-like photoexcitation of the moieties carried by the fluid. Imaging the microchannel flows carrying thus photoexcited chelates of lanthanide ions allowed us to extract their excited-state lifetimes from the spatial distribution of the changes in the emission intensity. The lifetime values obtained using this space-domain approach agreed well with the lifetimes from time-domain measurements. This validated space-domain microfluidic approach reveals a means for miniaturization of time-resolved emission spectroscopy.



Currently, the experimental determination of emission lifetimes requires time-domain or frequency-domain approaches.^{1,2} Time-domain measurements involve excitation with short pulses and monitoring of radiative decays with fast detectors.³ Conversely, frequency-domain measurements yield lifetimes from the phase shifts and the demodulation of emission signals recorded during photoexcitation with radio frequency-modulated illumination.⁴

Extracting temporal information from spatial distribution of optical signals benefited the development of ultrafast time-resolved spectroscopy. Pump–probe and streak-camera techniques utilizing a control of spatial delays for pulses (traveling with the speed of light) provide the means for pico- femto- and attosecond temporal resolution.^{5–9} Such ultrafast techniques, however, are unfeasible for nanosecond and longer time domains.

On the other side of the temporal range, mechanical chopper wheels provide a means for gating the excitation and the detection of radiative processes in the millisecond and second time domains.^{10–12} In fact, the use of chopper wheels for measurements of phosphorescence lifetimes of uranyl salts, reported by Alexandre-Edmond Becquerel in the mid 19th century,¹³ commenced the field of time-resolved spectroscopy. His son, Antoine Henri Becquerel, continued the work on time-resolved spectroscopy of uranium-containing compounds that lead to the discovery of radioactivity.^{14,15} The first chopper-wheel devices provided a means for measuring light-intensity

data points at time intervals of about 100 μ s, allowing for the determination of emission lifetimes as short as about 10 ms.¹³ Now, about 150 years later, the current technology permits the development of chopper wheels with electronically controlled kilohertz cycling frequency. Depending on the number and the width of the slots, the currently available chopper wheels allow not only for time-resolved emission measurements in the microsecond time domain but also for microsecond gating used for removing the fluorescence background from spectra and images utilizing photoprobes with relatively slow radiative decays.¹⁶

Attaching sample to the periphery of a rotating wheel provides an alternative for time-resolved emission measurements.^{17,18} Light focused at the periphery of the wheel results in strobe excitation as the turning disc carries the sample through the illuminated spot.¹⁸ Images of the turning wheel reveal a luminescence trace around its circumference. The intensity of the luminescent trace decreases as the sample turns away from the excitation spot.¹⁸ Converting spatial displacement to time provides a means for extracting the emission lifetimes of the rotating samples from the decrease in the intensity of the imaged luminescence.¹⁸

Received: January 19, 2013

Accepted: April 3, 2013

Published: April 3, 2013

Devices comprising chopper wheels or sample-holding discs, however, are not prone to miniaturization. Furthermore, the radii, the slot configurations, and the rotating frequencies of the wheels govern the limits of the feasibly attainable temporal resolution.

Microfluidics (μ FLs) presents an alternative for time-resolved spectroscopy by employing excitation and imaging (as detection), both operating solely in a steady-state mode.^{19–21} Flow velocities in the range of cm s^{-1} to m s^{-1} , readily attainable in μ FLs, provide the means for observable spatial displacement that correspond to micro- and millisecond time domains: i.e., time-domains that are too slow for ultrafast spectroscopy and too fast for traditional steady-state techniques.^{6,22} Inherently, μ FLs offers venues for miniaturization and for field-deployable technologies.

Fast mixing in microchannels, followed by monitoring the appearance of the microflows down the stream, allows for kinetic measurements with millisecond resolution.^{20,23,24} A control of the flow rates provides a means for converting the distance along an imaged microchannel into time scales.²³ In addition, the dynamics of plug-based microflows allows for introducing short strobe-like stimulations in minute reaction volumes.²⁵ The speed of mixing, the flow rates, and the spatial imaging resolution control the limits of the temporal resolution of such space-domain measurements. As an alternative, fluorescence lifetime imaging (where the difference in the emission lifetimes provides the imaging contrast) allows for monitoring the mixing processes in plug-based microflows with microsecond resolution.²⁶

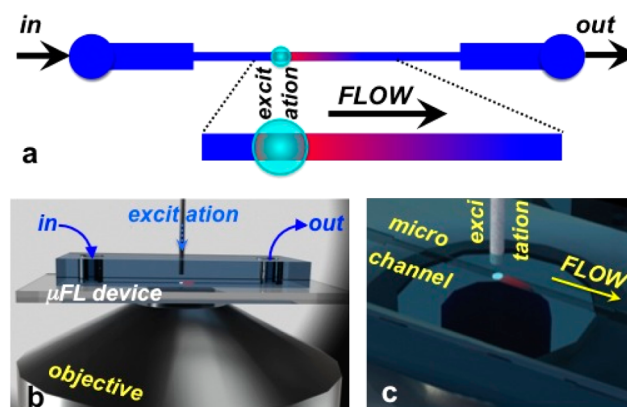
Pyridine-2,6-dicarboxylic acid, i.e., dipicolinic acid (DPA), is a natural product present solely in bacterial endospores^{27,28} and has a high affinity for lanthanide ions, Ln^{3+} .^{29,30} In such Ln^{3+} chelates, the DPA ligands act as photosensitizers, allowing access to spin-forbidden radiative-decay transitions of the chelated ions. Thus, the complexation of Tb^{3+} , Eu^{3+} , and other lanthanide ions with DPA, which enhances their emission, offers a key handle for biosensing of bacterial endospores.^{29,31–44} Furthermore, the emission lifetimes of such complexes strongly depend on the number of ligands chelating the metal ions.⁴⁵

The relatively long emission lifetimes of Ln^{3+} chelates has provided a means for suppressing the interference from background fluorescence in imaging and flow cytometry.⁴⁶ Using time gating allows for initiating the emission detection microseconds after the pulsed excitation, thus, eliminating the signals from the nanosecond radiative decays that do not necessarily involve intersystem crossing.^{47–49} The millisecond lifetimes of Tb^{3+} and Eu^{3+} chelates add readily obtainable temporal signatures for such Ln^{3+} -containing luminescent markers (in addition to their large-Stokes-shift spectral features).⁵⁰ In time-gated flow cytometry, offsetting the detection region downstream from the excitation spot results in a space-domain gating effect that additionally improves the detection of Ln^{3+} chelates without the contribution from the background fluorescence. These flow-cytometry applications, however, still employ time-modulated excitation sources, along with fast detectors with a relatively wide dynamic range, such as channel photomultipliers.^{16,48}

Overall, in time-gated flow cytometry, the fluid dynamics has provided a means for space-domain gating, based on long-lived excited states of Ln^{3+} chelates.⁴⁶ Using the dynamics of sample flows for extracting the characteristic lifetimes of photoexcited analytes, however, is still unexplored.

Herein, we explore the use of laminar microflows for time-resolved emission spectroscopy employing steady-state imaging. Continuous-waveform (CW) illumination of a short stretch of a microchannel caused a pulse-like excitation of chromophores carried by the flow through the illuminated region (Scheme 1). Epifluorescence imaging of microflows after such

Scheme 1. μ FL Setup for Space-Domain Measurements



- (a) Channel geometry;
(b) Device-microscope assembly;
(c) Close view of the working area of the device.

confined CW illumination revealed the progress of the radiative deactivation of the excited states of complexes of terbium, Tb^{3+} , and europium, Eu^{3+} , ions with DPA. Comparison of the obtained space-domain emission lifetimes with previously reported time-domain measurements^{37,45,51,52} revealed the unexplored benefits, as well as the limitations, of this microfluidic approach.

RESULTS

Principles of μ FL Space-Domain Spectroscopy. We hypothesized that if CW localized illumination at the beginning of a microchannel photoinitiates radiative processes, their progress can be monitored by imaging the microflows adjacent to the CW excitation. At flow rates, Q , of tens of microliters per minute, fluids move through microchannels in a laminar manner with average flow velocities, $\langle v \rangle$, on the order of decimeters per second (due to the small cross sections, A , of the channels): i.e., $\langle v \rangle = QA^{-1}$. Therefore, imaging such microflows with lateral resolution of a few micrometers provides the means for temporal resolution in the order of 10^{-5} s.

For the space-domain time-resolved emission measurements, we used print-and-peel (PAP)^{53–56} fabricated μ FL devices that were coupled with quartz optical fibers for illuminating small regions of the microchannels with UV light (Scheme 1a,c). As laminar flows carried solutions of Ln^{3+} and DPA through CW-illuminated spots, the chromophores experienced pulsed-like excitation (Scheme 1). Sufficiently fast flow velocities resulted in short enough effective durations of the flow-induced excitation pulses, ensuring that much of the radiative deactivation of the Ln^{3+} chelates occurred in the non-illuminated regions of the channels (Figure 1b). Images of such flows revealed green and red luminescence from the Tb^{3+} and Eu^{3+} solutions, respectively, decaying along the channel lengths after the illuminated spots.

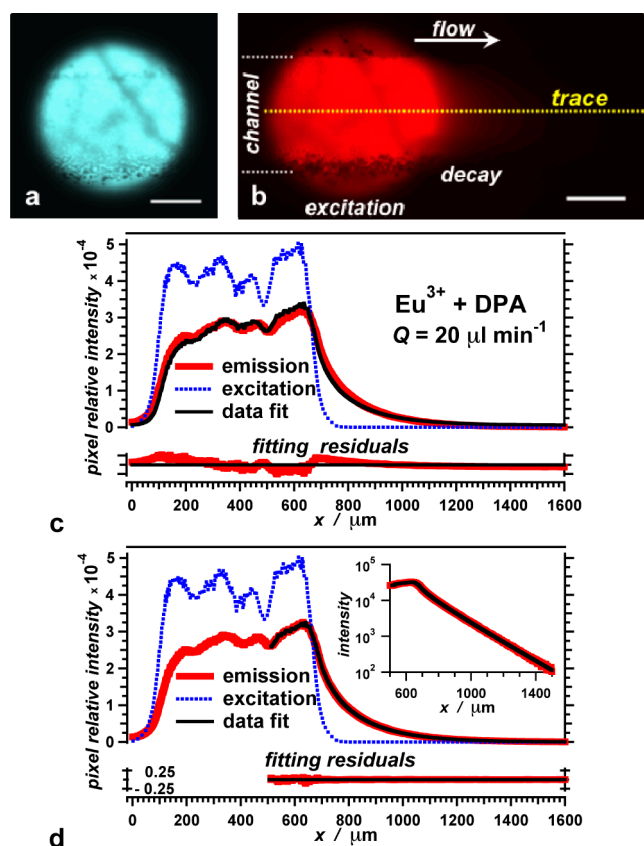


Figure 1. Space-domain time-resolved emission measurements. (a) Microscope image (16 bit) of the region of a microchannel, filled with water, illuminated at 280 nm. The imaged emission originated from autofluorescence. (b) Microscope image of the emission decay recorded through a band-pass filter (570–620 nm). Solution of 20 mM Eu^{3+} and 100 mM DPA was flown through the illuminated region of the channel ($\lambda_{\text{ex}} = 280 \text{ nm}$) at flow rate $Q = 20 \mu\text{L min}^{-1}$. Scale bars on parts a and b correspond to $200 \mu\text{m}$. (c) Emission trace, $R^*(x)$, extracted from the decay image, part b, along with excitation trace, $L(x)$, extracted from the image of the illumination spot, part a, and the data fit of $R^*(x)$ vs x using eqs 1 and 2. (d) The same $R^*(x)$ and $L(x)$ as part c, in which the data fitting was limited to the decay region of the image trace with minimum interference from the autofluorescence from the excitation spot. The difference in the lifetimes from parts c and d was less than 10%. The inset represents the decay data and the data fit plotted against the logarithmic ordinate. The use of eqs 1 and 2 provided adequate data fits for the traces, $R^*(x)$, extracted from images in part b. As indicated by the residuals, however, limiting the data fits to the regions of the emission-decay traces, $R^*(x)$, where the autofluorescence from the excitation had minimum to no contribution, improved the quality of the data fits, i.e., part c vs part d.

In general, PAP affords μFL channels with about $10\text{-}\mu\text{m}$ height, i.e., approximately 3 orders of magnitude smaller than the excitation pathways of 1-cm sample cuvettes that are regularly used in time-resolved spectroscopy.^{57–59} For the space-domain measurements, therefore, we employed millimolar sample concentrations in order to attain signal-to-noise ratios comparable to those of time-domain emission-decay data for micromolar solutions of Ln^{3+} chelates.⁴⁵

Two approaches allow spectral characterization of the emission-decays images: (1) separating the red, the green, and the blue components of RGB images recorded with a color camera and (2) placing band-pass filters between the μFL devices and a monochromatic camera, and imaging only the

spectral features at particular emission wavelength ranges. We used the latter approach because it provided improved selection of the wavelength ranges of interest.

Analysis of Time-Resolved Data in Space Domain.

Because the size of the excitation spots, $S(x, y)$, was comparable with the lengths of the imaged luminescence decays, we deconvoluted the measured emission response, $R^*(x, y)$, to extract the space-domain lifetimes, τ_s , of the samples (Figure 1c,d).^{60–65}

$$R^*(x, y) = R(x, y) + \psi S(x, y) \quad (1a)$$

$$\begin{aligned} R(x, y) &= \int_0^h L(x, y, z) \otimes G(x, y, z) dz \\ &= \int_0^h \int_0^x L(x - \xi, y, z) G(\xi, y, z) d\xi dz \end{aligned} \quad (1b)$$

where $R(x, y)$ is the response resultant from the chromophore emission, and the second term of the sum accounts for the imaged autofluorescence from the materials along the pathway of the excitation ultraviolet light. $L(x, y, z)$ is the intensity of the excitation light at coordinates x, y , and z , corresponding to the axes oriented along the length, the width, w , and the height, h , of the channel, respectively. $G(x, y, z)$ is an exponential decay function of emission induced by δ -function pulse excitation, i.e., excitation by illumination at a single point with coordinates $0, y, z$. This exponential decay function encompasses the conversion of spatial displacement along the channel length, x , to time after the δ -excitation, $t(y, z)$, employing the component of the flow velocity along x , $v_x(x, y, z)$:

$$L(x, y, z)_{0 \leq z \leq h} = S(x, y) 10^{-\varepsilon_{\text{ex}} C_{\text{DPA}}(h-z)} \quad (2a)$$

$$\begin{aligned} G(x, y, z) &= G_0 \exp\left(-\frac{t(y, z)}{\tau_s}\right) + g_\infty \\ &= G_0 \exp\left(-\frac{x}{v_x(x, y, z) \tau_s}\right) + g_\infty \end{aligned} \quad (2b)$$

The vertical z -dependence of L was estimated from the optical density of the samples by accounting for the concentration of DPA, C_{DPA} , i.e., the principal light absorber at 280 nm, and for its molar extinction coefficient at that wavelength, ε_{ex} (eq 2a).⁴⁵ For the image of the excitation spots, $S(x, y)$, we recorded the autofluorescence from the μFL devices without emissive sample in their channels (Figure 1a).

Flow-Velocity Profiles within Elastomer Microchannels. For flow rates between 10 and 50 mL min^{-1} , the Reynolds numbers, Re , for the aqueous solutions passing through the stretch of the microchannel illuminated with the excitation light ranged between 0.9 and 4.4. These relatively small values of Re ensured that the flows of the tested samples were laminar. Furthermore, because of the small heights of the channels, the entry lengths for the different flow rates did not exceed $10 \mu\text{m}$; i.e., the parabolic velocity profiles of the laminar flows were completely developed by the time they reached the illuminated region of the channels.

The conservation of mass allows for relating the flow-velocity profiles, $v(x, y, z)$, at each position x along the channel, with the flow rate, Q :

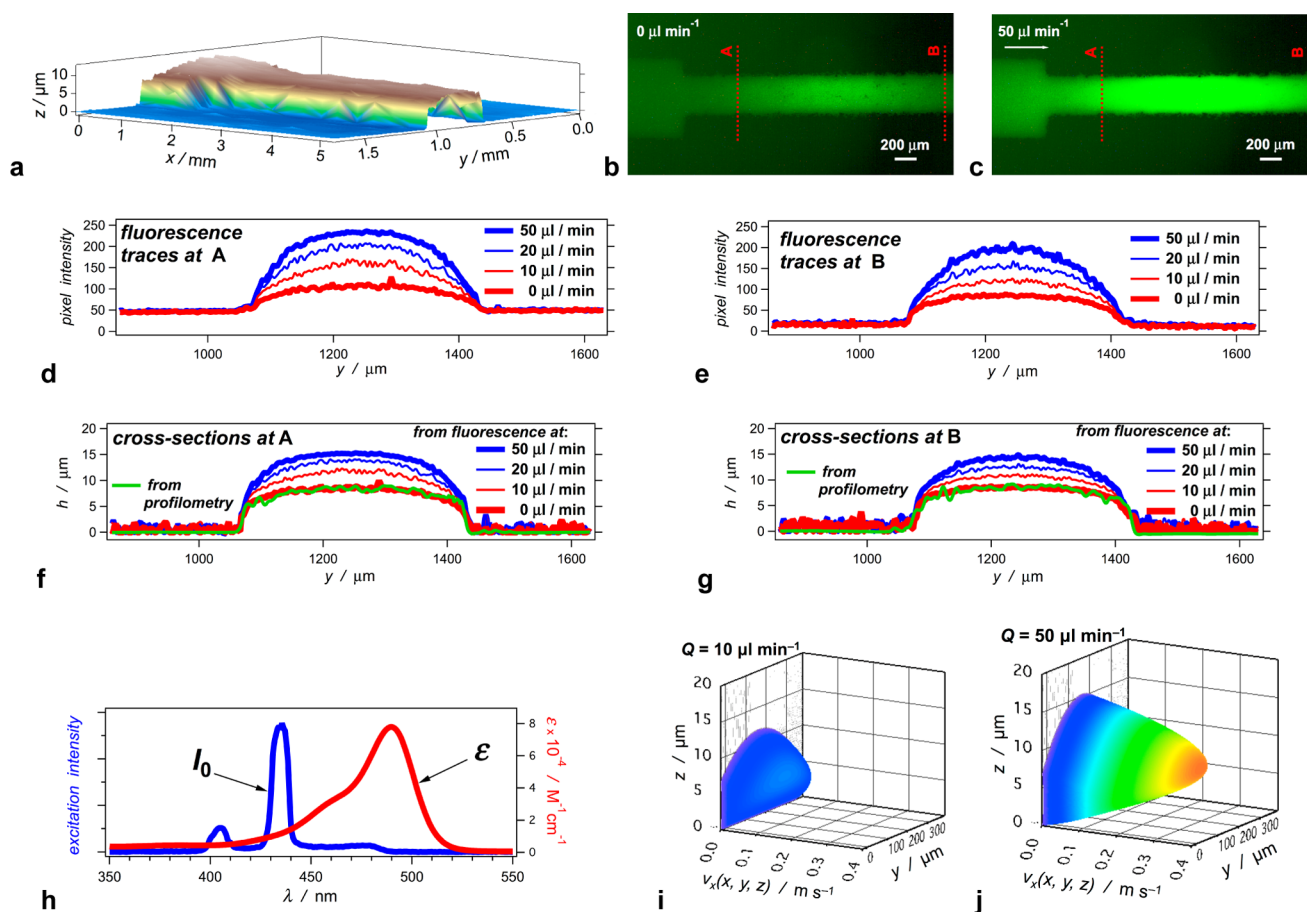


Figure 2. Channel cross-section and flow-velocity profiles, $v_x(x, y, z)$, estimated from profilometry and fluorescence images for different flow rates, Q . (a) Surface plot of the entrance region of a μ FL channel from profilometry data. (b, c) Uncorrected epifluorescence images (8 bit) of the entrance region of a μ FL channel filled with 1 mM aqueous solution of fluorescein buffered at pH 8, at rest and at flow rate of $50 \mu\text{L min}^{-1}$. (d, e) Uncorrected fluorescence traces across the channels, recorded at different flow rates, as indicated with the dotted red lines on the images, parts b and c. (f, g) Channel cross sections estimated from the fluorescence traces in parts d and e, using eqs 4 and 5. (h) Spectral overlap between the fluorescein absorption at pH 8 and the excitation, I_0 , obtained from the microscope mercury lamp as a light source, passed through the fluorescein isothiocyanate (FITC) excitation filter used for the recording of the fluorescence images. (i, j) Flow-velocity profiles for 10 and $50 \mu\text{L min}^{-1}$, obtained using eq 3 and smoothed cross sections (part f) for various flow rates assuming no-slip conditions and parabolic distribution.

$$Q = \int_0^w \int_0^h v(x, y, z) dz dy \approx \int_0^w \int_0^h v_x(x, y, z) dz dy \quad (3)$$

Dividing the x -coordinate by the magnitude of the components of the flow velocity vectors along the length of the channel, $v_x(x, y, z)$ provided the time-resolved features from the space-domain dynamics (eq 2b). Assuming parabolic distribution and no-slip conditions, we estimated the velocity-profile distributions across the channel cross sections from the flow rates (eq 3). Profilometry and fluorescence microscopy provided a means for determining the channel cross sections.

The μ FL devices were PAP-fabricated of poly-dimethylsiloxane (PDMS) slabs, permanently adhered to glass slides.^{66,67} Because of the relatively large elasticity of PDMS, pressure-driven flows deform the walls and the ceilings of the microchannels of such devices.⁶⁸ Such deformations alter the channel cross sections and the flow-velocity profiles during the operation of the devices. Therefore, profilometry measurements of the negative-relief imprints on the PDMS slabs (Figure 2a), prior to the device assembly, represented only of the channel cross sections with no pressure-driven flows through them.

Employing fluorescence microscopy allowed us to estimate the cross sections at different flow rates. We imaged the μ FL channels as we passed solution of fluorescein at different flow rates. An increase in the flow rate increased the intensity of the recorded emission from the imaged channels (Figure 2b,c). Because the dye concentration was constant, we ascribed this increase in the emission intensity to the increase in the thickness of the channel, i.e., to the increase in the pathway of excitation of the fluorescent sample.

The distribution of the imaged fluorescence intensity across the channels (at $0 \mu\text{L min}^{-1}$) does not directly follow the contour of the channel cross-section obtained from profilometry (Figure 2a,d,e). Unlike transmission optical microscopy where the recorded pixel intensity is linearly proportional to the height of the channel,⁵⁶ as well as to the concentration and the extinction coefficient of the chromophore, fluorescence intensity has a nonlinear dependence on these parameters.^{69,70} We, therefore, considered this nonlinearity in order to reconstruct the channel cross sections from the fluorescence images.

For estimating the shapes of the channel cross sections from the fluorescence images, we used data recorded with an objective that had a depth of field exceeding $\sim 30 \mu\text{m}$, i.e.,

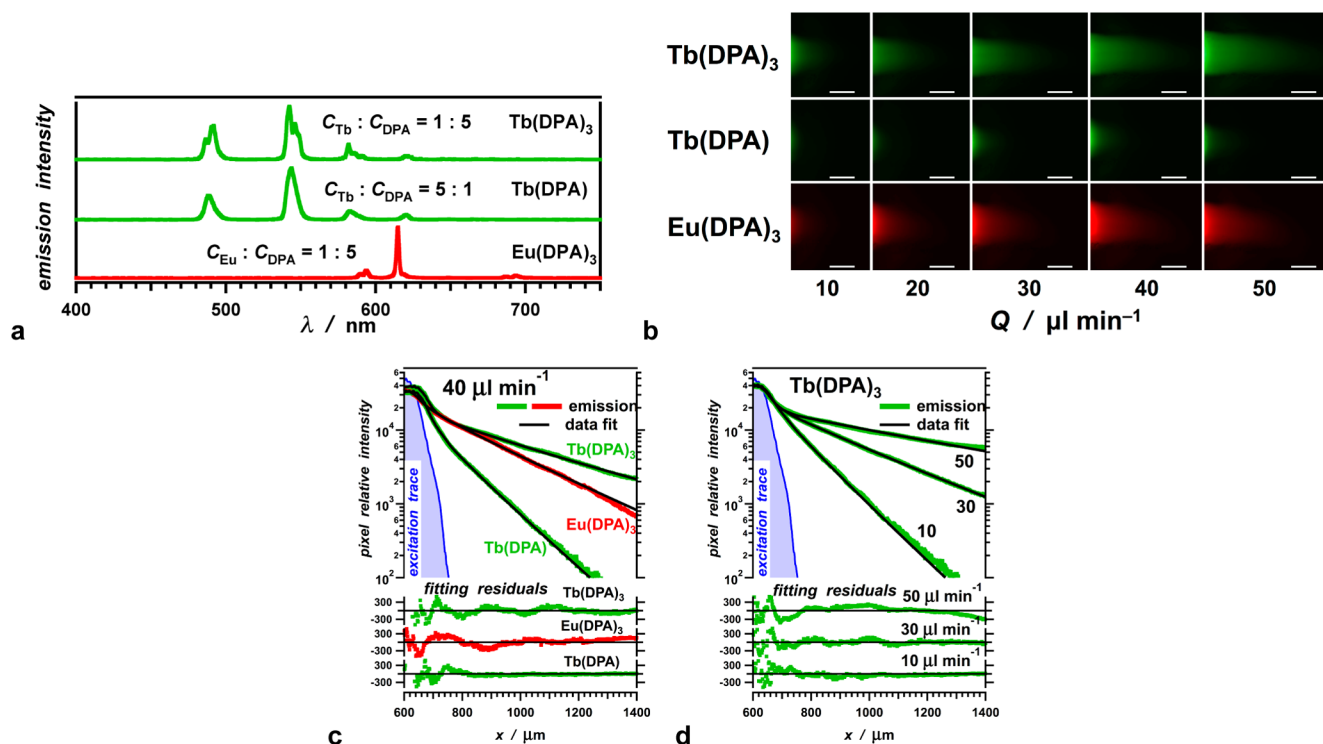


Figure 3. Space-domain emission decays of Tb³⁺ and Eu³⁺ chelated with DPA, recorded for different flow rates. (a) Emission spectra of Tb³⁺ and Eu³⁺ in the presence of DPA. (b) Images of the emission decays of lanthanide chelates, recorded at different flow rates. The scale bars correspond to 200 μm. The emission-decay images were recorded through band-pass filters: 510–560 nm for the terbium(III) samples and 570–620 nm for the europium(III) samples. (c) Emission-decay traces, $R^*(x)$, of the three lanthanide chelates recorded at flow rate, $Q = 40 \mu\text{L min}^{-1}$, along with the corresponding data fits and fitting residuals. (d) Emission-decay traces of Tb(DPA)₃, along with the corresponding data fits and fitting residuals, recorded at flow rates, $Q = 10, 30$, and $50 \mu\text{L min}^{-1}$. The traces were extracted from the middle of the imaged channels, i.e., $y = w/2$. For Ln(DPA)₃, $C_{\text{Ln}} = 20 \text{ mM}$ and $C_{\text{DPA}} = 100 \text{ mM}$; and for Tb(DPA), $C_{\text{Tb}} = 50 \text{ mM}$ and $C_{\text{DPA}} = 10 \text{ mM}$ ($\lambda_{\text{ex}} = 280 \text{ nm}$).

ensuring that the whole channel, $0 \leq z \leq h$, was within the depth of field. Therefore, we could represent the imaged fluorescence intensity, $F_{x,y}(h, \lambda_{\text{ex}})$, as an addition of the fluorescence from each point along the vertical axis, z , of the channel:

$$F_{x,y}(h, \lambda_{\text{ex}}) = \int_0^h F_{x,y}(z, \lambda_{\text{ex}}) dz \quad (4a)$$

where λ_{ex} is the excitation wavelength, and $F(z, \lambda_{\text{ex}})$ represents the fluorescence from an infinitesimally thin horizontal plane (with thickness $\zeta \rightarrow 0$), located at z . The fluorescence intensity is proportional to the emission quantum yield of the dye, Φ , and the light absorbed by the thin plane at z :

$$F(z, \lambda_{\text{ex}}) \propto \Phi I_0(\lambda_{\text{ex}})(1 - 10^{-\varepsilon(\lambda_{\text{ex}})C\zeta})10^{-\varepsilon(\lambda_{\text{ex}})Cz} \\ = I(\lambda_{\text{ex}})10^{-\varepsilon(\lambda_{\text{ex}})Cz} \quad (4b)$$

where $I_0(\lambda_{\text{ex}})$ is the light intensity at the bottom of the channel, i.e., at $z = 0$, $\varepsilon(\lambda_{\text{ex}})$ is the molar extinction coefficient of the dye, and C is the dye concentration. $I_0(\lambda_{\text{ex}})10^{-\varepsilon(\lambda_{\text{ex}})Cz}$ represents the intensity of the light transmitted through the dye solution from 0 to z , i.e., the intensity of the excitation light reaching the plane at z . The intensity of the absorbed light by the dye within the plane with thickness ζ is proportional to $(1 - 10^{-\varepsilon(\lambda_{\text{ex}})C\zeta})$, and $I(\lambda_{\text{ex}})$ does not have z -dependence, i.e., $I(\lambda_{\text{ex}}) = \Phi I_0(\lambda_{\text{ex}})(1 - 10^{-\varepsilon(\lambda_{\text{ex}})C\zeta})$. Substituting eq 4b in eq 4a and integrating along z provides the dependence of fluorescence on the channel height:

$$F_{x,y}(h, \lambda_{\text{ex}}) \propto I(\lambda_{\text{ex}}) \int_0^h 10^{-\varepsilon(\lambda_{\text{ex}})Cz} dz \\ = \frac{I(\lambda_{\text{ex}})\varepsilon(\lambda_{\text{ex}})C}{\ln(10)}(1 - 10^{-\varepsilon(\lambda_{\text{ex}})Ch}) \quad (4c)$$

$$F_{x,y}(h, \lambda_{\text{ex}}) = \varphi_{x,y} I(\lambda_{\text{ex}})\varepsilon(\lambda_{\text{ex}})(1 - 10^{-\varepsilon(\lambda_{\text{ex}})Ch}) \quad (4d)$$

The proportionality coefficient, $\varphi_{x,y}$, accounts for the dye quantum yield, for the microscope settings, and for the uneven illumination through the field of view. Because we employed broadband excitation for the microscopy measurements, we integrated eq 4b over the excitation wavelength range, between λ_1 and λ_2 , in order to relate the imaged fluorescence intensity with the channel height:

$$F_{x,y}(h) = \varphi_{x,y} Y(h) \quad (5a)$$

where

$$Y(h) = \int_{\lambda_1}^{\lambda_2} I(\lambda_{\text{ex}})\varepsilon(\lambda_{\text{ex}})(1 - 10^{-\varepsilon(\lambda_{\text{ex}})Ch}) d\lambda_{\text{ex}} \quad (5b)$$

We numerically solved the integral $Y(h)$, using $\varepsilon(\lambda)$ estimated from absorption spectra recorded for aqueous fluorescein solutions. For $I_0(\lambda_{\text{ex}})$, needed for calculating $I(\lambda_{\text{ex}})$, we used the spectrum of the mercury arc lamp of the fluorescence microscope, recorded through the excitation filter (Figure 2h). To calculate the proportionality coefficient, $\varphi_{x,y}$, we used the fluorescence recorded at no flow rate, $Q = 0$, and the channel heights obtained from profilometry measurements:

Table 1. Emission Lifetimes of Tb³⁺ and Eu³⁺ Chelates with DPA^a

chelate	τ_s/ms , measured at flow rates $Q/\text{mL min}^{-1b}$					$\langle\tau_s\rangle/\text{ms}^c$	τ_T/ms^d
	10	20	30	40	50		
Tb(DPA) ₃	2.13 ± 0.33	2.16 ± 0.23	1.98 ± 0.23	1.96 ± 0.27	1.99 ± 0.22	2.04 ± 0.26	2.05 ± 0.02
Tb(DPA)	0.581 ± 0.179	0.497 ± 0.183	0.556 ± 0.245	0.570 ± 0.152	0.531 ± 0.190	0.547 ± 0.192	0.528 ± 0.018
Eu(DPA) ₃	1.77 ± 0.37	1.64 ± 0.31	1.73 ± 0.27	1.56 ± 0.25	1.53 ± 0.31	1.65 ± 0.31	1.51 ± 0.11

^aData from four different microfluidic devices. For Ln(DPA)₃, $C_{\text{Ln}} = 20 \text{ mM}$ and $C_{\text{DPA}} = 100 \text{ mM}$; and for Tb(DPA), $C_{\text{Tb}} = 50 \text{ mM}$ and $C_{\text{DPA}} = 10 \text{ mM}$. ^bLifetimes, τ_s , from space-domain measurements. On the basis of a two factor ANOVA test, while the lifetime values were unique for each chelate, they did not depend on the flow rate, Q . The two null hypotheses were $H_0^{(1)}$, τ does not depend on the chelate; $H_0^{(2)}$, τ does not depend on Q . The p -values for the two hypotheses, obtained from the ANOVA test, were $p_{\text{chelate}} < 10^{-8}$, $p_Q = 0.57$, and $p_{\text{interaction}} = 0.93$. These findings allowed for rejecting $H_0^{(1)}$ but not $H_0^{(2)}$. ^cOn the basis of the lack of statistically significant dependence of the lifetimes on the flow rates, for each chelate, $\langle\tau_s\rangle$ is averaged over the five flow rates: $\langle\tau_s\rangle = 5^{-1} \sum_i \tau_s(Q_i)$. The error bars, $\Delta\tau_s$, were propagated from the error bars for the different flow rates: $\Delta\tau_s^2 = 5^{-1} \sum_i (\Delta\tau_s(Q_i))^2$. ^dLifetimes, τ_T , from time-domain measurements (from at least five different measurements for each of the chelates). On the basis of a Welch's t -test, i.e., a modified Student's t -test, the lifetimes obtained from space-domain, τ_s , and time-domain, τ_T , measurements did not differ within a 5% level of statistical significance, i.e., $\alpha = 0.05$. Testing H_0 , if τ_s and τ_T are identical for each of the three chelates, yielded $p = 0.87$, $p = 0.67$, and $p = 0.083$ for Tb(DPA)₃, Tb(DPA), and Eu(DPA)₃.

$$\varphi_{x,y} = \frac{F_{x,y,Q=0}(h_{\text{profilometry}})}{Y(h_{\text{profilometry}})} \quad (\text{Sc})$$

Applying eqs 4 and 5 to traces from the fluorescence images recorded at different flow rates, we estimated the cross section of the channels (Figure 2f,g). For channels with large aspect ratios, i.e., $w \gg h$,⁷¹ the fluorescence image data and finite element analysis revealed that the displacement and the arching of the channel ceilings (across the channel widths) encompasses the principal deformation that affects the cross sections and the flow-velocity profiles, which was in accordance with the report from Gervais et al.⁶⁸

Within the 2-mm stretch along the μFL channel, where we recorded the emission decays (Figure 1b), the difference between cross sections along the channel length, x , did not exceed $\sim 10\%$ (Figure 2f,g), which further justified the approximation $v(x, y, z) \approx v_x(x, y, z)$ in eq 3. Using the channel cross sections obtained from the fluorescence images, and employing no-slip conditions and parabolic distribution to eq 3, resulted in the flow-velocity profiles, $v_x(x, y, z)$, for different flow rates (Figure 2i,j), needed for the space-domain emission-decay analysis (eq 2).

Space-Domain Time-Resolved Emission of Ln³⁺ Chelates. Using the space-domain approach, we investigated the emission decays for mixtures of lanthanide ions and DPA, in which the luminescent species were a mono-chelated complex, i.e., Tb(DPA), and tris-chelated complexes, i.e., Tb(DPA)₃ and Eu(DPA)₃. In accordance with previous reports, solutions in which the concentration of the terbium ions, C_{Tb} , exceeded the DPA concentration 5-fold, provided predominantly mono-DPA chelates.^{30,45} Conversely, for the tris-chelated samples, the C_{DPA} exceeded the concentration of the lanthanide ions, C_{Ln} , 5-fold.^{45,52} The fine structure of the emission spectra of the Ln³⁺–DPA mixtures revealed that, indeed, for $C_{\text{Ln}}/C_{\text{DPA}} = 1:5$ the luminescent species were tris-chelates; and that for $C_{\text{Tb}}/C_{\text{DPA}} = 5:1$, the luminescent species were mono-chelates (Figure 3a).^{45,52}

For all samples, the principal light absorber was DPA: at 280 nm, the molar extinction coefficients of Tb³⁺ or Eu³⁺ are considerably smaller than that of DPA.⁴⁵ The photoexcited DPA moieties that ligated the lanthanide ions, Ln³⁺, undergo fast energy transfer to Ln³⁺, while the photoexcited free DPA molecules undergo nonradiative deactivation. Thus, the principal luminophores in the Ln³⁺–DPA solutions were the chelated Tb³⁺ and Eu³⁺.

For the space-domain emission measurements, we passed the Ln³⁺–DPA solutions through the illuminated channels with flow rates ranging from 10 to 50 $\mu\text{L min}^{-1}$ (Figure 3b). An increase in the flow rate increased the lengths of the emission decays (Figure 3b,d) and hence improved the temporal resolution. The backpressure, however, sets the principal limit on the maximum flow rates that were feasibly attainable. Furthermore, at the same flow rate, the lengths of the emission decays from the three chelates differed (Figure 3b,c) in accordance with the differences in their luminescence lifetimes.^{37,45,51,52,72}

From recorded images of $R^*(x, y)$ and $S(x, y)$, we extracted traces along the middle of the channels, reducing the data to a one-dimensional spatial coordinate that provides the time resolution, i.e., $R^*(x)_{y=w/2}$ and $S(x)_{y=w/2}$ (Figure 1). Least-square (LS) fits of the $R^*(x)$ traces using eqs 1 and 2, and the estimated flow-velocity profiles (Figure 2), allowed for extracting the emission decay lifetimes for solutions containing luminescent lanthanide chelates (Figure 1c,d). The fitting parameters encompassed the lifetime, τ_s , along with other quantities, G_0 , ψ , and g_∞ (eqs 1, 2), that were not available via alternative estimates. For each flow rate, the terbium tris-chelate samples exhibited the longest lifetimes and the terbium mono-chelate samples, the shortest (Table 1). For each chelate, the lifetimes extracted from the emission-decay traces did not manifest statistically significant dependence on the flow rate (Table 1, footnote b²²). The thus obtained values of τ_s were in good agreement with the previously reported lifetimes of these chelates.^{37,45,51,52,72}

To further confirm the emission lifetimes obtained from the space-domain image data, we examined the luminescence properties of the same Ln³⁺ samples using time-domain measurements. Illuminating the samples with femtosecond pulses from a modelocked laser source resulted in emission decay signals that extended to a few milliseconds after the excitation (Figure 4). The laser pulse-width was orders of magnitude smaller than the measured lifetimes, ensuring that δ -function represented a reasonable approximation for the excitation pulses. Monoexponential fits of these time-domain emission-decay data yielded lifetimes, τ_T , that agreed well with the space-domain measured τ_s (Table 1, footnote d).

DISCUSSION

The steady-state mode of operation, employed in this space-domain μFL approach allowed for a fast acquisition of

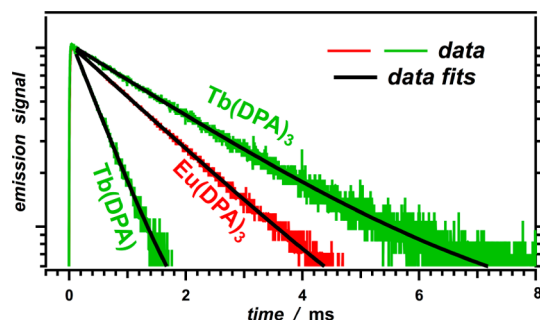


Figure 4. Time-domain measurements, with the corresponding monoexponential data fits, of emission decays of Tb^{3+} and Eu^{3+} chelated with DPA, normalized for $t = 0$, which correspond to the timing of the excitation laser pulse and presented against the logarithmic ordinate. For $\text{Ln}(\text{DPA})_3$, $C_{\text{Ln}} = 20 \text{ mM}$ and $C_{\text{DPA}} = 100 \text{ mM}$; and for $\text{Tb}(\text{DPA})$, $C_{\text{Tb}} = 50 \text{ mM}$ and $C_{\text{DPA}} = 10 \text{ mM}$ ($\lambda_{\text{ex}} = 266 \text{ nm}$; 40 fs pulse width at 800 nm prior to the second and third harmonic generators).

emission-decay data with relatively large signal-to-noise ratios. Using lanthanide chelates as emission samples, we demonstrated the feasibility of employing facily fabricated microdevices for measuring lifetimes that range from hundreds of microseconds to milliseconds.

It took seconds to record the emission-decay images using easy-to-fabricate low-cost μFL assemblies. Furthermore, this space-domain approach provides venues for miniaturization, allowing for *in situ* time-resolved spectroscopy measurements on lab-on-a-chip (LoC) setups. In fact, the fluorescence microscope was the “bulkiest” component of the setup needed for these studies. The development of the camera and microscopy field-deployable technologies, however, will address concerns for competitive cost and size of the microscopes needed for the space-domain μFL measurements.^{73,74} Even in these studies, the cost and the size of the equipment for time-domain measurements (Figure 4) exceeded the cost and the size of the space-domain emission microscopy setup.

Implementing time-domain measurements in microfluidics by employing “traditional” time-correlated single-photon counting (TCSPC), indeed, provides venues for reducing of the sample size.^{75,76} In addition to requiring pulsed excitation and fast detectors, however, such time-domain measurements do not take advantage of the flow dynamics in the microchannels. On the contrary, for samples with relatively long-lived excited states, fast flow rates may result in unacceptably short residence times of the photoexcited chromophores in the detection area. (The useful residence time in the detection area spans between the excitation pulse and the moment when the flow carries the chromophores out of the region where the emission is monitored.) The residence time should considerably exceed the measured emission lifetime, τ_{T} . If the residence time is shorter than the emission lifetime, the measurements will yield τ_{T} that is biased toward smaller values.

Furthermore, TCSPC measurements may take an hour or longer to acquire reasonable counts per channel for decays in the hundreds of microsecond and millisecond domains. Therefore, space-domain time-resolved emission spectroscopy, which is based on steady-state measurements, has certain unexplored advantages that can prove useful for a range of analytical and LoC applications.

Average flow velocities of decimeters per second provide the means for temporal resolutions of 10 μs or better assuming micrometer optical spatial resolution between neighboring points on the decay images. In the current devices, however, the size of the excitation spot (Figure 1a) sets the lower limit on the measurable lifetimes. For the flow velocities we attained (Figure 2), excitation spanning over 300 μm along the channel prevented the characterization of emission-decay kinetics with lifetimes much smaller than about 100 μs . Therefore, decreasing the area of the excitation spot would not only extend the lower limit of the measurable lifetimes but also simplify the analysis of emission decays involving relatively long lifetimes by eliminating the need for spatial deconvolution (eq 1b).

An increase in the flow rate lengthened the decay traces (Figure 3b) and appeared to provide the means for improving not only the temporal resolution but also the lower limit of the attainable lifetimes. Such a flow-rate increase, however, also increased the backpressure, which deformed the channels and increased the areas of the cross sections, decreasing the average flow velocity in comparison with nondeformed channels. Therefore, the elasticity of the polymer composing the devices presented a limitation on the feasibly useful flow-rate range.

As a material for fabricating μFL devices, PDMS has a range of disadvantages, such as pronounced elasticity and oxygen permeability.^{77,78} Indeed, employing nonelastic materials for space-domain devices would not only prevent the deformation of the microchannels but also considerably simplify the analysis of the flow-velocity profiles and improve the dynamic range for the measurements, which will make this technique even more attractive than the herein proof-of-concept design.

Nevertheless, the ease of molding, along with the simplicity of assembling microdevices, has made PDMS one of the most widely used material for μFL devices.^{79–84} Indeed, PAP-fabricated PDMS microdevices allowed us to demonstrate the concept of space-domain time-resolved spectroscopy.

CONCLUSIONS

Simplicity and speed are some of the attractive features of this space-domain microfluidic technique. While probing emission decays in femtosecond to nanosecond time domains is routine for the developed time-resolved spectroscopy techniques, monitoring radiative processes in the microsecond and millisecond scales is challenging for most of these “traditional” approaches. Indeed, custom assemblies of Q-switched pulsed lasers, reasonably fast photodetectors, and oscilloscopes provide access to the microsecond and millisecond time domains.^{37,45} Conversely, the space-domain μFL approach offers accessible means for exploring millisecond and submillisecond photokinetics, i.e., time domains important for biochemical probes⁸⁵ and for emerging nanomaterials.⁸⁶ We believe that such space-domain approach will provide key venues for bringing time-resolved spectroscopy to lab-on-a-chip settings.

EXPERIMENTAL SECTION

Materials. Terbium(III) chloride hexahydrate (99.999%), europium(III) chloride hexahydrate (99.999%), and pyridine-2,6-dicarboxylic acid were purchased from Sigma-Aldrich. Glacial acetic acid and aqueous ammonium hydroxide solution were obtained from Fisher Scientific. Polydimethylsiloxane (PDMS), prepolymer and curing agent, was obtained from Dow Corning. Microscope glass slides were purchased from

Fisher Scientific. Nonradiopaque polyethylene tubing was purchased from BD Medical.

For the chelate solutions, preweighed amounts of DPA and lanthanide salts were separately dissolved in Milli-Q water. Ammonium hydroxide was added dropwise to the DPA solution to bring the pH close to 7 and to ensure complete dissolution.⁹ Acetic acid was added to the lanthanide chloride solutions to bring the pH to 6.5–7 and to prevent the formation of precipitates of the metal hydroxide.⁹ Each of the lanthanide solutions was mixed with the corresponding DPA solution. Upon the formation of white precipitate, either ammonia solution or acetic acid was added to bring the pH to 7 and hence redissolve the precipitate. The thus prepared DPA–lanthanide solutions were diluted with Milli-Q water to attain the targeted concentrations for the microfluidic time-resolved emission measurements.

Device Fabrication. We fabricated the devices using PAP as we have previously described.^{53–56} The CAD pattern of the microchannel was prepared using Adobe Illustrator (v. 14.0.0). Using a laser-jet printer (Hewlett-Packard Laser-Jet 1320), the designed patterns were printed on overhead transparency films to form positive-relief masters. Upon immobilization of the master films to the bottom of polystyrene Petri dishes, polyethylene posts for forming of inlet and outlet vertical channels were immobilized at the termini of the printed channel patterns.^{53,56} About 0.5 mm film of PDMS prepolymer-curing agent mixture was added and allowed to cure.

To form the well for the excitation source, a polypropylene cylinder was placed on the cured PDMS film above the microchannels for space-domain measurements. Quartz optical fibers, coupled with UV LEDs (FIALab LED-Lamp 280 nm), were used for the excitation source. Hence, the diameter of the polypropylene-cylinder molds corresponded to the diameter of the termini of the optical fibers. An additional 5 mm layer of PDMS prepolymer mixture was poured over the cured elastomer with posts and cylinders on it and allowed to cure. Upon curing of the second layer of PDMS, the elastomer slabs were lifted from the printed transparency masters and the polymer posts were removed from the slabs to leave inlet and outlet channels and a well for the optical fiber over each horizontal microchannel imprint. The slabs were cut into 10 mm × 25 mm blocks (each block encompassing one test microchannel with an inlet, an outlet, and a well for an optical-fiber terminus) to form the PDMS components of the devices. The PDMS surfaces with the negative microchannel imprints were activated with oxygen plasma (50 W, 0.5 mbar)^{21,22} and permanently adhered to glass slides to yield the microfluidic devices for space-domain measurements.

The cross-section of the channels was determined prior to adhering the PDMS slabs to the glass, using a benchtop surface profilometer (Dektak 8, Veeco Systems). The 9-mm long test channels under the excitation-illuminated area had $7.5 \pm 0.5 \mu\text{m}$ height and $365 \pm 10 \mu\text{m}$ width. Two 3-mm long, 0.7-mm wide channels connected the test channels with the inlet and the outlet (Scheme 1a).

Estimating Flow-Velocity Profiles. The estimation of the velocity profiles and especially of the velocity profiles in the middle of the channels, $v_x(x, y=w/2, z)$ needed for analyzing the decay traces (Figures 1b–d and 3b–d), involved (1) estimation of the cross sections of the channels in the emission-decay regions and (2) numerical calculation of $v_x(x, y, z)$ from the cross sections and the flow rates, Q (eq 3).

For estimating the channel cross sections in absence of flows, a benchtop surface profilometer (Dektak 8, Veeco Systems), with 12.5- μm radius stylus, was employed for the analysis of the negative-relief channel imprints on the PDMS surfaces. To reconstruct the channel shapes (Figure 2a), usually 1.6-mm scans across the channel imprints were performed at every 0.2 mm, 5-mm along the channel length.

For reconstructing the channel cross sections under flow conditions, 1 mM aqueous fluorescein solution (buffered at pH 8 with 10 mM phosphate buffer) was passed through the channel at different flow rates and imaged with an AcuScope 3031 inverted fluorescence microscope equipped with a FITC filter and Spot Insight digital CCD camera.

From the epifluorescence images of the channels, the cross sections of the channels were reconstructed using eqs 4 and 5. For the proportionality coefficient, $\varphi_{x,y}$, we assumed negligible alteration of the excitation illumination intensity across the channel for each cross section, i.e., $\varphi_{x,y} \approx \varphi_x$. Using eq 5c, therefore, we estimated φ_x for each cross section from the profilometry data and the imaged fluorescence values for the middle of the channel, i.e., for $y = w/2$.

Considering the maximum channel height, h_{max} , extracted from the cross sections and that the principal deformation involved curving of the PDMS ceiling (Figure 2f,g), the shape of the deformed cross sections, in terms of the height of the channels, $h(y)$, at various points y along the width, was estimated

$$h(y) = h_{\text{max}} - r + \sqrt{r^2 - \left(y - \frac{w}{2}\right)^2} \quad (6a)$$

where r is the radius of the circular arc representing the ceiling deformation:

$$r = \frac{4(h_{\text{max}} - h_0)^2 + w^2}{8(h_{\text{max}} - h_0)} \quad (6b)$$

Approximating the shape of the arc from circular to parabolic allows for simplifying the expression for $h(y)$:

$$h(y) \approx h_0 + (h_{\text{max}} - h_0) \left(1 - \left(\frac{2y - w}{w}\right)^2\right) \quad (6c)$$

At each y value (along the width), the flow-velocity profiles were modeled as parabolically distributed $v_x(x, y, z)$ along the height of the channels, z , with maximum velocity in the half-height, and zero velocity at the floor and the ceiling, i.e., $v_x(x, y, z = h/2) = v_{\text{max}}(x, y)$, and $v_x(x, y, z = h) = v_x(x, y, z = 0) = 0$.⁷¹ Near the side edges of the flat channels, i.e., $y < h/2$ and $y > w - h/2$, $v_{\text{max}}(x, y)$ had a parabolic distribution along y ;⁷¹ and in the absence of any deformation, $v_{\text{max}}(x, y)$ was constant for $h/2 < y < w - h/2$. At each point y for deformed channels, $v_{\text{max}}(x, y)$ was increased proportionally with $h(y)$. Using these considerations for the y, z distribution of the flow-velocity values across the cross sections of the deformed channels, for each coordinate x along the flow with different rates, Q , the flow-velocity profiles, v_x , were calculated numerically using eq 3.

Space-Domain Time-Resolved Emission Measurements. The space-domain emission decays of microflows, containing lanthanide chelates, were imaged using a Nikon Eclipse Ti-S fluorescence microscope equipped with a 10× Nikon CFI Plan Fluor objective lens and a Hamamatsu EM-CCD camera (model C9100-13).^{70,87–89} Band-pass filters were placed on the optical pathway between the device and the

camera: 510–560 nm for the terbium(III) samples and 570–620 nm for the europium(III) sample. For the excitation spots (Figure 1a), the illuminated region was imaged without band-pass filters and without lanthanide(III) samples in the channels. The photoexcitation was delivered by placing the illumination source (UV LED-coupled optical fiber) in the well.

For recording excitation profiles, $S(x, y)$, the channels were filled with Milli-Q water and the autofluorescence of the assembly was imaged at $Q = 0 \mu\text{L min}^{-1}$. The same $S(x, y)$ profiles were obtained when the channels were filled with aqueous solutions of fluorophores, such as fluorescein, with nanoseconds excited-state lifetimes. For recording the emission-response profiles, $R^*(x, y)$, the solution was passed through the microchannel at flow rates, Q , of 10, 20, 30, 40, and $50 \mu\text{L min}^{-1}$ using a programmable syringe pump (Harvard Apparatus PHD 2000). At each flow rate for each chelate solution, the images of the decay flows were captured with exposure time of 10 s using HCLImage Hamamatsu imaging software (the sensitivity gain was set to 0, and the gain was set to 1).

Because the field of view of the objective was $0.5 \text{ mm} \times 0.5 \text{ mm}$, several images displaced along the channel were recorded in order to encompass the complete emission decay patterns. Using Photomerge (with Reposition layout and no photo-correction options selected) as implemented with Adobe Photoshop (v. 11.0; CS4 extended), the monochromatic square images were overlapped and merged together to generate the continuous decay patterns without further manipulations.

Data Analysis. From the monochromatic images, the emission-decay traces, $R^*(x, y)$ and the excitation traces, $S(x, y)$, were extracted from the middle of the channels as gray scale intensity of the pixels vs the channel length, x (Figure 1), as we have previously demonstrated.⁵⁶ Using a least-squares data-fitting algorithm, as implemented by Igor Pro (v. 6.02A),^{90–93} the emission lifetimes were extracted from the emission-decay traces using the space-domain deconvolution function (eqs 1, 2).

To illustrate the concepts behind the spectral differences of the space-domain emission data recorded through different optical filters, some of the monochromatic images were colored using Adobe Photoshop CS4. A new layer, filled with either red color (RGB value of R:255 G:0 B:0) or green color (RGB value of R:0 G:200 B:0) color to show europium(III) or terbium(III) luminescence, respectively, was created over the original TIFF files and modified using the Overlay layer blending option. These images (Figures 1b and 3b) were created solely to demonstrate the concept behind the space-domain spectroscopy and were not used for extracting the decay traces and emission lifetimes.

Time-Domain Time-Resolved Emission Measurements. The laser source for the pulsed excitation was a SpitFire Pro 35F regenerative amplifier (Spectra Physics/Newport) generating 800-nm pulses (38 fs, 4 mJ, 55 nm bandwidth) at 1 kHz repetition rate. The amplifier was pumped with an Empower 30 Q-switched laser ran at 20 W and a MaiTai SP oscillator provided the seed beam. The 800-nm beam was passed through a second-harmonic and a third-harmonic generator (MiniOptic Technology, Inc., Arcadia, CA), and the repetition rate of the 266-nm beam was reduced from 1 kHz to about 33 Hz.

The emission was detected at 90° to the excitation illumination. The liquid samples were placed in a quartz cuvette in front of a Si detector with a nanosecond response

time equipped with the appropriate band-pass optical filters. The signals from the photodetector were forwarded to a 300-MHz digital oscilloscope (LeCroy 9361) and terminated at 50Ω , resulting in the recorded emission-decay traces (Figure 4).^{45,94}

Emission Spectroscopy. Steady-state emission spectra (Figure 3a) were recorded using a FluoroLog-3 spectrofluorometer (Horiba-Jobin-Yvon) equipped with double-grating monochromators and a TBX single-photon-counting detector ($\lambda_{\text{ex}} = 280 \text{ nm}$).^{95–97} To suppress the detection of the $2 \times \lambda_{\text{ex}}$ signal, a long-pass filter ($\lambda_{\text{cutoff}} = 380 \text{ nm}$) was placed on the optical pathway between the cuvette and the emission monochromator. By adjusting the slit widths, the signal at all wavelengths was kept under 10^6 CPS to ensure that it was within the linear dynamic range of the detector.

AUTHOR INFORMATION

Corresponding Author

*Address: Department of Bioengineering, Material Science and Engineering Building, Room 235, University of California, Riverside, CA 92521. Fax: +1 951 827 6416. Phone: +1 951 827 6239. URL: <http://www.vullevgroup.ucr.edu/>. E-mail: vullev@ucr.edu.

Present Addresses

[†]B.M.: Department of Biomedical Engineering, Johns Hopkins University School of Medicine, Baltimore, MD 21205.

[‡]G.Y.G.: Department of Natural Sciences, Assumption College, Worcester, MA 01609.

Notes

The authors declare no competing financial interest.

ACKNOWLEDGMENTS

This research was supported by the U.S. National Science Foundation (Grants CBET 0923408 and CBET 0935995 as well as Grant GRFP 2011081805 for V.N. and Grant IGERT DGE 0903667 for J.M.L.) and by the Riverside Public Utilities. We also extend our gratitude to Prof. Victor G. J. Rodgers and Prof. Jerome S. Schultz for assisting with the fluid-dynamics analysis, to Prof. Bahman Anvari for providing access to the imaging equipment in his lab, to Prof. Lorenzo Mangolini for providing the silicon detector for the time-domain measurements, to Ms. Teodora Bozhilova for assisting with the graphic design, and to Prof. B. Hyle Park for insightful discussions regarding the image analysis.

REFERENCES

- (1) Lakowicz, J. R. *Principles of Fluorescence Spectroscopy*, 3rd ed.; Springer Science+Business Media, LLC: New York, 2006.
- (2) Wróbel, D.; Dudkowiak, A.; Goc, J. *Rev. Fluoresc.* **2010**, *5*, 237–275.
- (3) Birch, D. J. S.; Imhof, R. E. *Top. Fluoresc. Spectrosc.* **1991**, *1*, 1–95.
- (4) Gratton, E.; Jameson, D. M.; Hall, R. D. *Annu. Rev. Biophys. Bioeng.* **1984**, *13*, 105–124.
- (5) Campillo, A. J.; Shapiro, S. L. *IEEE J. Quantum Electron.* **1983**, *QE-19*, 585–603.
- (6) Beeby, A. In *Introduction to Laser Spectroscopy*, 2nd ed.; Andrews, D. L., Demidov, A. A., Eds.; Kluwer Academic/Plenum Publishers: New York, 2002; pp 105–137.
- (7) Fushitani, M. *Annu. Rep. Prog. Chem., Sect. C: Phys. Chem.* **2008**, *104*, 272–297.
- (8) Nisoli, M.; Sansone, G. *Prog. Quantum Electron.* **2009**, *33*, 17–59.
- (9) Wan, J.; Ferreira, A.; Xia, W.; Chow, C. H.; Takechi, K.; Kamat, P. V.; Jones, G.; Vullev, V. I. *J. Photochem. Photobiol. A: Chem.* **2008**, *197*, 364–374.

- (10) Berezin, M. Y.; Achilefu, S. *Chem. Rev.* **2010**, *110*, 2641–2684.
- (11) Sutherland, J. C.; Cimino, G. D.; Desmond, E. J. *Anal. Biochem.* **1979**, *97*, 158–165.
- (12) Parker, C. A.; Hatchard, C. G. *Analyst* **1962**, *87*, 644–676.
- (13) Becquerel, E. *Ann. Chim. Phys.* **1859**, *55*, 5–128.
- (14) Becquerel, H. *Comptes Rendus* **1896**, *122*, 420–421.
- (15) Becquerel, H. *Comptes Rendus* **1896**, *122*, 501–503.
- (16) Jin, D. Y.; Piper, J. A. *Anal. Chem.* **2011**, *83*, 2294–2300.
- (17) Wood, R. W. *Proc. R. Soc. London, Ser. A: Math. Phys. Charact.* **1921**, *99*, 362–371.
- (18) Jones, B. T.; Smith, B. W.; Berthod, A.; Winefordner, J. D. *Talanta* **1988**, *35*, 647–650.
- (19) Ristenpart, W. D.; Wan, J.; Stone, H. A. *Anal. Chem.* **2008**, *80*, 3270–3276.
- (20) Song, H.; Chen, D. L.; Ismagilov, R. F. *Angew. Chem., Int. Ed.* **2006**, *45*, 7336–7356.
- (21) Mayers, B. T.; Vezenov, D. V.; Vullev, V. I.; Whitesides, G. M. *Anal. Chem.* **2005**, *77*, 1310–1316.
- (22) Thomas, M. S.; Nuñez, V.; Upadhyayula, S.; Zielins, E. R.; Bao, D.; Vasquez, J. M.; Bahmani, B.; Vullev, V. I. *Langmuir* **2010**, *26*, 9756–9765.
- (23) Song, H.; Ismagilov, R. F. *J. Am. Chem. Soc.* **2003**, *125*, 14613–14619.
- (24) Bringer, M. R.; Gerdt, C. J.; Song, H.; Tice, J. D.; Ismagilov, R. F. *Phil. Trans. R. Soc. London, Ser. A: Math., Phys. Eng. Sci.* **2004**, *362*, 1087–1104.
- (25) Chen, D.; Du, W. B.; Liu, Y.; Liu, W. S.; Kuznetsov, A.; Mendez, F. E.; Philipson, L. H.; Ismagilov, R. F. *Proc. Natl. Acad. Sci. U.S.A.* **2008**, *105*, 16843–16848.
- (26) Solvas, X. C. L.; Srisa-Art, M.; Demello, A. J.; Edel, J. B. *Anal. Chem.* **2010**, *82*, 3950–3956.
- (27) Setlow, P. Resistance of Bacterial Spores. In *Bacterial Stress Responses*, 2nd ed.; Storz, G., Hengge, R., Eds.; ASM Press: Washington, DC, 2011; pp 319–332.
- (28) Slieman, T. A.; Nicholson, W. L. *Appl. Environ. Microbiol.* **2001**, *67*, 1274–1279.
- (29) Cable, M. L.; Kirby, J. P.; Levine, D. J.; Manary, M. J.; Gray, H. B.; Ponce, A. J. *Am. Chem. Soc.* **2009**, *131*, 9562–9570.
- (30) Jones, G., II; Vullev, V. I. *J. Phys. Chem. A* **2002**, *106*, 8213–8222.
- (31) Rosen, D. L.; Sharpless, C.; McGown, L. B. *Anal. Chem.* **1997**, *69*, 1082–1085.
- (32) Pellegrino, P. M.; Fell, N. F., Jr.; Rosen, D. L.; Gillespie, J. B. *Anal. Chem.* **1998**, *70*, 1755–1760.
- (33) Rosen, D. L. *Appl. Opt.* **1998**, *37*, 805–807.
- (34) Hindle, A. A.; Hall, E. A. H. *Analyst* **1999**, *124*, 1599–1604.
- (35) Rosen, D. L. *Rev. Anal. Chem.* **1999**, *18*, 1–21.
- (36) Rosen, D. L. *Appl. Opt.* **2006**, *45*, 3152–3157.
- (37) Cable, M. L.; Kirby, J. P.; Sorasane, K.; Gray, H. B.; Ponce, A. J. *Am. Chem. Soc.* **2007**, *129*, 1474–1475.
- (38) Yung, P. T.; Lester, E. D.; Bearman, G.; Ponce, A. *Biotechnol. Bioeng.* **2007**, *98*, 864–871.
- (39) Yung, P. T.; Shafaat, H. S.; Cannon, S. A.; Ponce, A. *FEMS Microbiol. Ecol.* **2007**, *59*, 300–306.
- (40) Li, Q.; Dasgupta, P. K.; Temkin, H. K. *Environ. Sci. Technol.* **2008**, *42*, 2799–2804.
- (41) Yung, P. T.; Ponce, A. *Appl. Environ. Microbiol.* **2008**, *74*, 7669–7674.
- (42) Yang, W.-W.; Ponce, A. *Int. J. Food Microbiol.* **2009**, *133*, 213–216.
- (43) Yang, W.-W.; Ponce, A. *Appl. Environ. Microbiol.* **2011**, *77*, 2352–2358.
- (44) Ammann, A. B.; Kölle, L.; Brandl, H. *Int. J. Microbiol.* **2011**, *2011*, No. 435281.
- (45) Jones, G., II; Vullev, V. I. *Photochem. Photobiol. Sci.* **2002**, *1*, 925–933.
- (46) Jin, D. Y. *Methods Cell Biol.* **2011**, *102*, 479–513.
- (47) Jin, D. Y.; Connally, R.; Piper, J. *Cytometry, Part A* **2007**, *71A*, 783–796.
- (48) Jin, D.; Connally, R.; Piper, J. *Cytometry, Part A* **2007**, *71A*, 797–808.
- (49) Gahlaut, N.; Miller, L. W. *Cytometry, Part A* **2010**, *77A*, 1113–1125.
- (50) Jones, G., II; Yan, D. *Compositions and methods for luminescence lifetime comparison*. U.S. Patent 6,402,986, June 11, 2002.
- (51) Horrocks, W. D. J.; Sudnick, D. R. *Science* **1979**, *206*, 1194–1196.
- (52) George, M. R.; Golden, C. A.; Grossel, M. C.; Curry, R. J. *Inorg. Chem.* **2006**, *45*, 1739–1744.
- (53) Vullev, V. I.; Wan, J.; Heinrich, V.; Landsman, P.; Bower, P. E.; Xia, B.; Millare, B.; Jones, G., II. *J. Am. Chem. Soc.* **2006**, *128*, 16062–16072.
- (54) Hong, C.; Bao, D.; Thomas, M. S.; Clift, J. M.; Vullev, V. I. *Langmuir* **2008**, *24*, 8439–8442.
- (55) Thomas, M. S.; Millare, B.; Clift, J. M.; Bao, D.; Hong, C.; Vullev, V. I. *Ann. Biomed. Eng.* **2010**, *38*, 21–32.
- (56) Thomas, M. S.; Clift, J. M.; Millare, B.; Vullev, V. I. *Langmuir* **2010**, *26*, 2951–2957.
- (57) Xia, B.; Bao, D.; Upadhyayula, S.; Jones, G.; Vullev, V. I. *J. Org. Chem.* **2013**, *78*, 1994–2004.
- (58) Jones, G., II; Vullev, V. I. *J. Phys. Chem. A* **2001**, *105*, 6402–6406.
- (59) Jones, G., II; Vullev, V.; Braswell, E. H.; Zhu, D. J. *Am. Chem. Soc.* **2000**, *122*, 388–389.
- (60) Giurleo, J. T.; Talaga, D. S. *J. Chem. Phys.* **2008**, *128*, 114114/114111–114114/114118.
- (61) Lu, H.; Bao, D.; Penchev, M.; Ghazinejad, M.; Vullev, V. I.; Ozkan, C. S.; Ozkan, M. *Adv. Sci. Lett.* **2010**, *3*, 101–109.
- (62) Jones, G., II; Vullev, V. I. *Org. Lett.* **2001**, *3*, 2457–2460.
- (63) Jones, G., II; Vullev, V. I. *Org. Lett.* **2002**, *4*, 4001–4004.
- (64) Jones, G., II; Zhou, X.; Vullev, V. I. *Photochem. Photobiol. Sci.* **2003**, *2*, 1080–1087.
- (65) Ghazinejad, M.; Kyle, J. R.; Guo, S.; Pleskot, D.; Bao, D.; Vullev, V. I.; Ozkan, M.; Ozkan, C. S. *Adv. Funct. Mater.* **2012**, *22*, 4519–4525.
- (66) Millare, B.; Thomas, M.; Ferreira, A.; Xu, H.; Holesinger, M.; Vullev, V. I. *Langmuir* **2008**, *24*, 13218–13224.
- (67) Chau, K.; Millare, B.; Lin, A.; Upadhyayula, S.; Nuñez, V.; Xu, H.; Vullev, V. I. *Microfluid. Nanofluid.* **2011**, *10*, 907–917.
- (68) Gervais, T.; El-Ali, J.; Guenther, A.; Jensen, K. F. *Lab Chip* **2006**, *6*, 500–507.
- (69) Wan, J.; Thomas, M. S.; Guthrie, S.; Vullev, V. I. *Ann. Biomed. Eng.* **2009**, *37*, 1190–1205.
- (70) Xia, B.; Upadhyayula, S.; Nuñez, V.; Landsman, P.; Lam, S.; Malik, H.; Gupta, S.; Sarshar, M.; Hu, J.; Anvari, B.; Jones, G.; Vullev, V. I. *J. Clin. Microbiol.* **2011**, *49*, 2966–2975.
- (71) Spiga, M.; Morini, G. L. *Int. Commun. Heat Mass Transfer* **1994**, *21*, 469–475.
- (72) Latva, M.; Takalo, H.; Mukkala, V.-M.; Matachescu, C.; Rodriguez-Ubis, J. C.; Kankare, J. J. *Luminesc.* **1997**, *75*, 149–169.
- (73) Breslauer, D. N.; Maamari, R. N.; Switz, N. A.; Lam, W. A.; Fletcher, D. A. *PLoS One* **2009**, *4*, e6320.
- (74) Zhu, H. Y.; Isikman, S. O.; Mudanyali, O.; Greenbaum, A.; Ozcan, A. *Lab Chip* **2013**, *13*, 51–67.
- (75) Cleary, A.; Glidle, A.; Laybourn, P. J. R.; Garcia-Blanco, S.; Pellegrini, S.; Helfter, C.; Buller, G. S.; Aitchison, J. S.; Cooper, J. M. *Appl. Phys. Lett.* **2007**, *91*, 071123-1–071123-3.
- (76) Ohla, S.; Beyreiss, R.; Fritzsche, S.; Glaser, P.; Nagl, S.; Stockhausen, K.; Schneider, C.; Belder, D. *Chem.—Eur. J.* **2012**, *18*, 1240–1246.
- (77) Houston, K. S.; Weinkauf, D. H.; Stewart, F. F. J. *Membr. Sci.* **2002**, *205*, 103–112.
- (78) Mehta, G.; Lee, J.; Cha, W.; Tung, Y.-C.; Linderman, J. J.; Takayama, S. *Anal. Chem.* **2009**, *81*, 3714–3722.
- (79) McDonald, J. C.; Whitesides, G. M. *Acc. Chem. Res.* **2002**, *35*, 491–499.
- (80) Gates, B. D. *Mater. Today* **2005**, *8*, 44–49.

- (81) Hui, A. Y. N.; Wang, G.; Lin, B.; Chan, W.-T. *Lab Chip* **2005**, *5*, 1173–1177.
- (82) Pan, T.; Wang, W. *Ann. Biomed. Eng.* **2011**, *39*, 600–620.
- (83) Fiddes, L. K.; Raz, N.; Srigunapalan, S.; Tumarkan, E.; Simmons, C. A.; Wheeler, A. R.; Kumacheva, E. *Biomaterials* **2010**, *31*, 3459–3464.
- (84) Teh, S.-Y.; Lin, R.; Hung, L.-H.; Lee, A. P. *Lab Chip* **2008**, *8*, 198–220.
- (85) Thomas, D. D.; Carlsen, W. F.; Stryer, L. *Proc. Natl. Acad. Sci. U.S.A.* **1978**, *75*, 5746–5750.
- (86) Sykora, M.; Mangolini, L.; Schaller, R. D.; Kortshagen, U.; Jurbergs, D.; Klimov, V. I. *Phys. Rev. Lett.* **2008**, *100*, 067401/067401–067401/067404.
- (87) Upadhyayula, S.; Quinata, T.; Bishop, S.; Gupta, S.; Johnson, N. R.; Bahmani, B.; Bozhilov, K.; Stubbs, J.; Jreij, P.; Nallagatla, P.; Vullev, V. I. *Langmuir* **2012**, *28*, 5059–5069.
- (88) Gupta, S.; Chatni, M. R.; Rao, A. L. N.; Vullev, V. I.; Wang, L. V.; Anvari, B. *Nanoscale* **2013**, *5*, 1772–1776.
- (89) Bahmani, B.; Gupta, S.; Upadhyayula, S.; Vullev, V. I.; Anvari, B. *J. Biomed. Opt.* **2011**, *16*, 051303/051301–051303/051310.
- (90) Vullev, V. I.; Jones, G. *Tetrahedron Lett.* **2002**, *43*, 8611–8615.
- (91) Jones, G., II; Yan, D.; Hu, J.; Wan, J.; Xia, B.; Vullev, V. I. *J. Phys. Chem. B* **2007**, *111*, 6921–6929.
- (92) Bao, D.; Ramu, S.; Contreras, A.; Upadhyayula, S.; Vasquez, J. M.; Beran, G.; Vullev, V. I. *J. Phys. Chem. B* **2010**, *114*, 14467–14479.
- (93) Upadhyayula, S.; Bao, D.; Millare, B.; Sylvia, S. S.; Habib, K. M. M.; Ashraf, K.; Ferreira, A.; Bishop, S.; Bonderer, R.; Baqai, S.; Jing, X.; Penchev, M.; Ozkan, M.; Ozkan, C. S.; Lake, R. K.; Vullev, V. I. *J. Phys. Chem. B* **2011**, *115*, 9473–9490.
- (94) Vullev, V. I.; Jones, G., II *J. Appl. Sci.* **2005**, *5*, 517–526.
- (95) Bao, D.; Millare, B.; Xia, W.; Steyer, B. G.; Gerasimenko, A. A.; Ferreira, A.; Contreras, A.; Vullev, V. I. *J. Phys. Chem. A* **2009**, *113*, 1259–1267.
- (96) Hu, J.; Xia, B.; Bao, D.; Ferreira, A.; Wan, J.; Jones, G.; Vullev, V. I. *J. Phys. Chem. A* **2009**, *113*, 3096–3107.
- (97) Vasquez, J. M.; Vu, A.; Schultz, J. S.; Vullev, V. I. *Biotechnol. Prog.* **2009**, *25*, 906–914.